Journal of Astronomical Telescopes, Instruments, and Systems

AstronomicalTelescopes.SPIEDigitalLibrary.org

Detection and characterization of circumstellar material with a WFIRST or EXO-C coronagraphic instrument: simulations and observational methods

Glenn Schneider
Dean C. Hines

SPIE.

Glenn Schneider, Dean C. Hines, "Detection and characterization of circumstellar material with a WFIRST or EXO-C coronagraphic instrument: simulations and observational methods," *J. Astron. Telesc. Instrum. Syst.* **2**(1), 011022 (2016), doi: 10.1117/1.JATIS.2.1.011022.

Downloaded From: http://astronomicaltelescopes.spiedigitallibrary.org/ on 01/14/2017 Terms of Use: http://spiedigitallibrary.org/ss/termsofuse.aspx

Detection and characterization of circumstellar material with a WFIRST or EXO-C coronagraphic instrument: simulations and observational methods

Glenn Schneider[a,*] and Dean C. Hines[b]
[a]The University of Arizona, Steward Observatory and the Department of Astronomy, North Cherry Avenue, Tucson, Arizona 85712, United States
[b]Space Telescope Science Institute, 3700 San Martin Drive, Baltimore, Maryland 21218, United States

Abstract. The capabilities of a high ($\sim 10^{-9}$ resel^{-1}) contrast narrow-field coronagraphic instrument (CGI) on a space-based WFIRST-C or probe-class EXO-C/S mission are particularly and importantly germane to symbiotic studies of the systems of circumstellar material from which planets have emerged and interact with throughout their lifetimes. The small particle populations in "disks" of co-orbiting materials can trace the presence of planets through dynamical interactions that perturb the spatial distribution of light-scattering debris, which is detectable at visible wavelengths and resolvable with a WFIRST-C or EXO-S/C CGI. Herein, we (1) present the scientific case to study the formation, evolution, architectures, diversity, and properties of the material in the planet-hosting regions of nearby stars; (2) discuss how a CGI under current conception can uniquely inform and contribute to those investigations; (3) consider the applicability of CGI-anticipated performance for circumstellar debris system studies; (4) investigate, through WFIRST CGI image simulations, the anticipated interpretive fidelity and metrical results from specific representative zodiacal debris disk observations; (5) comment on specific observational modes and methods germane to and augmenting circumstellar debris system observations; and (6) present a case for augmenting future CGI instrumentation with the capability to obtain full linear-Stokes imaging polarimetery, which greatly benefits characterization of the material properties of circumstellar dust and exoplanet atmospheres (discussed in other studies). *© 2016 Society of Photo-Optical Instrumentation Engineers (SPIE)*
[DOI: 10.1117/1.JATIS.2.1.011022]

Keywords: circumstellar disks; circumstellar dust; coronagraphy; high-contrast imaging; polarimetry.

Paper 15033SS received Jun. 1, 2015; accepted for publication Mar. 14, 2016; published online Apr. 15, 2016.

1 Introduction

Circumstellar materials in "disks" orbiting stars are both the progenitors and the outcomes of planetary system formation processes. NASA's Kepler mission and ground-based radial velocity and transit programs have recently made huge strides toward a census of and statistical expectations for exoplanets and exoplanetary systems. However, a deeper understanding of the complex nature of exoplanetary system formation, evolution, architectures, composition, and diversity requires studying material in the circumstellar planet-hosting and interacting environments at all size scales co-orbiting with planets or escaping the systems, and over a wide range of stellocentric distances.

Our solar system possesses a two-component circumstellar debris system, with the outer Edgeworth-Kuiper belt (EKB) region of cold dust ($T_{\mathrm{dust}} \sim 30$ to 40 K) co-located with the domain of the giant planets and beyond (to ~60 AU), and the inner zodiacal disk region of warm dust ($T_{\mathrm{dust}} \sim 80$ to 400 K) within the zone of the terrestrial planets, the Sun's habitable zone, and the main asteroid belt. Whether such two-component architectures are typical or not is largely unknown, since direct imaging of terrestrial disks has yet to be accomplished with current technologies.

The difficulty in assessing how typical our solar system is can be illustrated by considering an external observer investigating the solar system. The infrared (IR) emission from the circumstellar debris in our solar system relative to the total photospheric emission from the Sun is $L_{\mathrm{IR}}/L_{\mathrm{star}} \sim 10^{-7}$. If viewed from outside the solar system at visible wavelengths, this circumstellar material would have a disk-integrated scattered starlight fraction of $f_{\mathrm{disk}}/f_{\mathrm{star}} \sim 4 \times 10^{-8}$, with spatially resolved surface brightness dependent on viewing geometry. The challenge is suppressing the central starlight enough to make such faint scattered light detectable.

Herein, we define image contrast as the ratio of the flux density contained within a resolution element at any stellocentric angular distance from the central star to the flux density within the central resolution element of the unsuppressed stellar point spread function (PSF) core. As for $L_{\mathrm{IR}}/L_{\mathrm{star}}$, $f_{\mathrm{disk}}/f_{\mathrm{star}}$ is proportional to the total dust mass in the circumstellar disk system. The spatial distribution of such dust, however, will depend on the architecture of the planetary system, which is likely to be different from our own system given the diversity in planetary system architectures found by Kepler.

High spatial resolution visible to near-IR imaging observations of the outer EKB-analog regions of approximately two dozen circumstellar disk systems have been obtained over the past two decades, mostly with the Hubble Space Telescope (HST). Surface brightness measurements of these disks suggest, through models constrained by thermal spectral energy distributions, systemic dust masses many thousands of times that of our

*Address all correspondence to: Glenn Schneider, E-mail: gschneider@as.arizona.edu

2329-4124/2016/$25.00 © 2016 SPIE

Downloaded From: http://astronomicaltelescopes.spiedigitallibrary.org/ on 01/14/2017 Terms of Use: http://spiedigitallibrary.org/ss/termsofuse.aspx

EKB. These same observations have also revealed a remarkable diversity in morphologies and architectures in these outer detectable regions (e.g., see Ref. 1). However, the inner zodiacal-belt analog regions currently remain incognita due to instrumental sensitivity and inner working angle (IWA) limitations (see Fig. 1). Such light-scattering circumstellar disk systems may be probed into their zodiacal-belt regions with a WFIRST or EXO-C coronagraphic instrument (CGI), and we can use these previously observed systems to guide our plans for using a WFIRST or EXO-C CGI.

2 Key Disk Science Questions Addressable with a WFIRST or EXO-C CGI

The currently conceived WFIRST CGI raw image contrast ($\sim 10^{-9}$ resel^{-1}) with order of magnitude postprocessing improvement at subarcsecond stellocentric IWAs will, for the first time, uniquely enable spatially resolved imaging into the zodiacal and co-spatial habitable zone warm dust regions around nearby stars. This leads directly to the ability to explore some key questions in exoplanetary system science, including:

- What are the levels of circumstellar dust in and exterior to the habitable zones of exoplanetary systems?

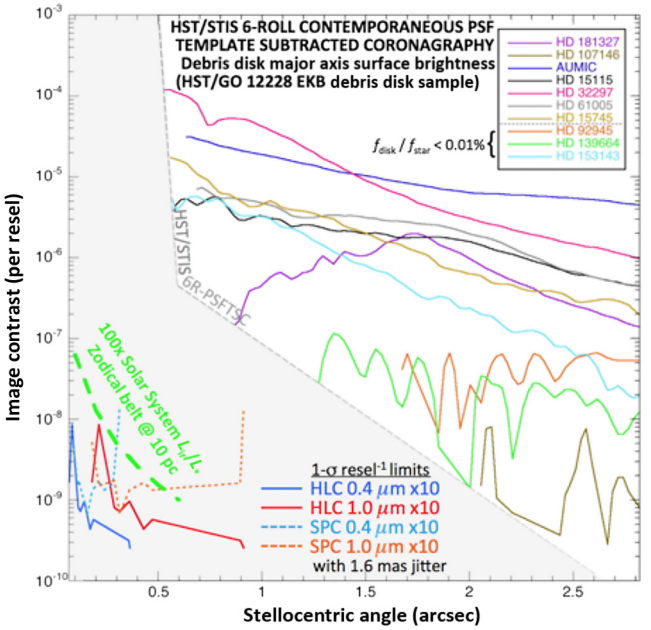

Fig. 1 Top right region above gray dashed line: visible light surface brightness profiles of 10 of 24 circumstellar debris systems imaged to date (see Fig. 1 for corresponding images), measured along their disk major axes. The most favorable (f_{disk}/f_{star} brightest) systems that are currently observable are traced to stellocentric major axis IWAs $\approx$ 0.5 to 0.7 arcsec (not smaller physical mask limits due to HST observational systematics) but only at contrast levels $>5 \times 10^{-5}$ resel^{-1} commensurate with massive EKB-analog disks in the stellocentric regions accessible. Fainter (and larger) EKB-analog only disks are observable at smaller contrast levels, but only at larger stellocentric distances (bottom right). Bottom left region below the gray dashed line: CGI 3-σ resel^{-1} detection limits for circumstellar material in red and blue channels with anticipated $\times$10 contrast augmentation via speckle calibration in 10 h integration. This puts zodiacal disks (solar system analog with $\sim$100$\times$ more dust in green) well within the grasp of either WFIRST HLC or SPC.

- Will dust in habitable zones interfere with future planet-finding attempts?
- How do dust substructures trace the presence of (unseen) planets?
- What veneer is delivered to planetary atmospheres and surfaces by asteroids, comets, and other circumstellar material?

And, extended to the inner regions of transitional and protoplanetary disks:

- How do disks of protoplanetary materials evolve to make solar system–like architectures?

The answers to these and other related, highly compelling, and fundamental questions may be forthcoming through direct imaging that informs theoretical models imposing wavelength-dependent constraints via filter photometry and/or integral field unit (IFU) spectroscopy, both also benefiting from polarimetry (see Sec. 8). The former are the baseline observational modes for a currently conceived WFIRST CGI, integrating a high-performance wavefront error control system and high-contrast coronagraph for starlight suppression. These proposed capabilities provide access to the inner regions of starlight-scattering circumstellar disks in previously inaccessible observational domains of contrast and IWA.

3 Starlight-Scattering Circumstellar Dust in Exoplanetary Systems

How planetary systems, including our own, form and evolve is one of the most fundamental and compelling areas of inquiry in contemporary astrophysics. Over the last few decades, visible, IR, and (sub)millimeter observations have shown that most stars are surrounded at birth by circumstellar disks of primordial material. Separately, today, $\sim$700 exoplanet candidates have been detected by radial velocity techniques and more than five times as many by Kepler transit photometry. These planets are thought to originate in such disks, with Jovian-mass planets forming before circumstellar disks become gas-poor over time.

The evolutionary transformation of gas-rich disks to systems with small amounts of dust and little residual gas occurs over the first $\sim$10 Myr of the star's lifetime, with warm dust ($T_{dust} > \sim$160 K) rare after $\sim$3 Myr. Much of the dust may then be tied up in the formation of smaller rocky or icy bodies that can interact with co-orbiting giant planets or smaller bodies and collide, which will replenish the circumstellar environments with second-generation material. Such collisional replenishment of dust-rich circumstellar particles can continue throughout the lifetime of the system. In our own solar system, even after 4.6 Gyr, this process is evidenced by the presence of the zodiacal dust cloud, the asteroid belt, and the EKB.

The dust in the circumstellar debris systems absorbs stellar radiation that is then reradiated at thermal IR to millimeter wavelengths. It also scatters this light at visible and near-IR wavelengths. Even cold particles ($T_{dust} \sim$ 30 to 40 K) far from their parent stars are illuminated by starlight. Scattered-light images of cold dust regions, such as those imaged with HST, have thus far provided the greatest insights, because they have traced dust over a wide range of stellocentric distances at high spatial resolution. For example, visual-to-near-IR coronagraphic images of the star HR 4796A show a narrow EKB-analog region ring that may be shepherded and dynamically

Downloaded From: http://astronomicaltelescopes.spiedigitallibrary.org/ on 01/14/2017 Terms of Use: http://spiedigitallibrary.org/ss/termsofuse.aspx

sculpted by unseen planets.[2,3] Coronagraphic images of the circumstellar disk associated with the Herbig AeBe star HD 141596 reveal spiral and/or arc-like substructures in its observable EKB-analog region with an inner gap indicative of the dynamical effects of an embedded giant planet.[4–7] Such geometries and features are proving to be common in spatially resolved scattered-light images of circumstellar disk systems. However, no instrument yet built has the IWA and imaging contrast necessary to detect and spatially resolve zodiacal disks where temperatures allow liquid water to remain on a planet's surface.[8] Such extra-solar zodiacal disk analogs would be observable with a WFIRST or EXO-C CGI.

Planets set the locations where planetesimal belts and their debris can stably persist. The maintenance of the inner edge of our EKB by Neptune[9] and the inclination of β Pic b to its warped, or two-component, debris disk are among the very few directly observable examples of dynamic links between planets and circumstellar debris systems. A WFIRST or EXO-C CGI will uniquely provide detailed information about these circumstellar debris systems and their architectures even if individual planets remain elusive.

4 Imaging Circumstellar Material—L_{IR}/L_{star} Expectations

Evidence of circumstellar material possibly associated with planet formation and subsequent evolution came with the detection of thermal IR emission above stellar photospheric brightness levels, with $L_{IR}/L_{star} \approx 2 \times 10^{-3}$ for stars such as Vega and β Pictoris. These initial detections with IRAS (Ref. 10) were interpreted as arising from reradiation of absorbed stellar light by orbiting debris particles and later confirmed by the first spatially resolved image of the prototypical light-scattering circumstellar debris disk of β Pictoris.[11]

Fractional IR luminosity (L_{IR}/L_{star}) is dependent upon the particle properties (e.g., size, composition, structure) and stellocentric distance, and is an easily measurable quantity. In an optically thin medium, as may be expected for dust in a circumstellar debris system, L_{IR}/L_{star} is proportional to the systemic dust mass, and thus is a commonly used metric for choosing objects that should be detectable at other wavelengths and in scattered light.

Hundreds of such posited dust-bearing systems were identified through their thermal excesses as measured with IRAS. However, direct imaging examples in scattered light of circumstellar debris systems with the largest L_{IR}/L_{star} (other than β Pic) remained elusive until the era of space-based coronagraphy with HST.[1,6,12,13] Even then, HST surveys for light-scattering circumstellar debris systems with visible and near-IR coronagraphy of systems with $L_{IR}/L_{star} \geq \sim 10^{-4}$ returned imaging detections of only ~15%. Therefore, L_{IR}/L_{star} alone is not a strong predictor of visual/near-IR scattered-light surface brightness in the absence of constraints otherwise informed by systemic geometries and particle properties.

The two-component circumsolar debris system in the solar system has an L_{IR}/L_{star} of $\approx 10^{-7}$, so an object with $L_{IR}/L_{star} = 10^{-4}$ could have ~1000× the circumstellar dust found in our solar system. Viewed face-on from 10 pc, the solar system would have an optical light-scattering fraction, f_{disk}/f_{star}, of $\sim 4 \times 10^{-8}$. While correlation with scattered-light surface brightness depends on dust properties, spatial distribution, and line-of-sight inclination, for a true solar system analog circumstellar debris system with 1000× dust mass, one would expect an f_{disk}/f_{star} of $\approx 4 \times 10^{-5}$ for a face-on system, which is approximately at the limit of HST subarcsecond IWA capabilities at visible wavelengths with space telescope imaging spectrograph (STIS).

Recent visible-light HST coronagraphic observations of a sample of the outer regions of 10 circumstellar debris systems show a remarkable diversity in disk morphologies and substructures from 0.3 arcsec outward. Unfortunately, the inner regions of these systems, analogous to the zodiacal belt in our solar system, are beyond even the capabilities of HST and ground-based extreme adaptive optics (AO) systems.

5 Coronagraphic Instrument Zodiacal-Analog Disk Targets vis-à-vis Science Goals

A WFIRST or EXO-C CGI will enable spatially resolved imaging of zodiacal-analog disks into stellar habitable zones, where liquid water can exist on planetary surfaces. With augmented image contrasts of $\sim 10^{-9}$ resel^{-1}, the selection of targets for imaging in zodiacal-analog disks can be unbiased by stellar ages for nearby systems with sufficiently large amounts of warm dust ($L_{IR}/L_{star} \geq$ few × 10 of our solar system, with T_{dust} a few hundred Kelvins).

What are the levels and nature of the dust in the habitable zones of exoplanetary debris systems? The CGI spatial resolution enables mapping of the two-dimensional spatial distribution of zodiacal-analog disk dust of sufficient scattered-light surface brightness (see Sec. 7 for WFIRST CGI examples). Radially differentiated image structure (surface brightness, color, and polarization) informs on stellocentric segregation of particles with temperature-dependent properties. Azimuthal asymmetries in dust surface brightness distributions, beyond those attributable to scattering phase functions, inform on possible perturbations (resonances, sculpting, pericentric offsets of dust features, and so on) caused by co-orbiting planets that may or may not be detectable (e.g., see Sec. 7.4), but can be modeled to constrain planetary orbits and masses.

Will dust in habitable zones interfere with planet-finding? The amount of dust in the habitable zone around other stars is critical in determining the best strategies to later image Earth-like planets, since light scattered by circumstellar dust is the main source of astrophysical noise in detecting such faint embedded point sources.

The masses measured for protoplanetary disks are typically lower than the mass needed to form the planets in the Solar System.[14] Since the amount of debris disk emission is proportional to and decays from the initial mass in the corresponding protoplanetary disks,[15] these results together suggest that the absence of debris dust in an evolved system may indicate that it had a low-mass protoplanetary disk to begin with. It is therefore at least conceivable that by targeting stars without debris dust, future exoplanet imaging missions may be selecting targets unlikely to have had sufficient initial mass for rich planetary systems. That is, optimal strategies for imaging Earth-like planets in habitable zones may have to balance competing considerations about circumstellar debris. Doing so requires a deep understanding of the prevalence and evolution of debris dust, an understanding that simply cannot be achieved with the limited number of systems currently imaged.

Primary samples for consideration in building a WFIRST CGI disk-science Design Reference Mission thus include (1) the nearby stars that are (a) distance-limited and (b) have radial velocity detected exoplanets; (2) circumstellar debris

Downloaded From: http://astronomicaltelescopes.spiedigitallibrary.org/ on 01/14/2017 Terms of Use: http://spiedigitallibrary.org/ss/termsofuse.aspx

systems with previously imaged EKB-analog region disks; (3) light-scattering circumstellar debris system candidates from newly identified long-wavelength excesses and imaging; (4) young stars hosting known protoplanetary disks. We comment further on items (1) through (3).

5.1 *Nearby FGK Stars*

In Fig. 2, we show the stellocentric reach of the WFIRST CGI's proposed B and Z filter bands (see Table 1) with respect to zodiacal-analog disks extending outer zodiacal disk radii of 6 AU and their corresponding habitable zones for F, G, and K stars in a distance-limited sample with <25 pc. We adopt habitable zone limits between 0.8 and 1.8 AU, scaled by sqrt$(L_{\rm star}/L_{\rm sun})$. We also scale the outer distance of the zodiacal dust based loosely on our solar system; the actual dust distribution will depend upon the individual exoplanetary system architectures. The target stars plotted in Fig. 2, with zodiacal-analog disk regions accessible to a WFIRST CGI, do not represent an $L_{\rm IR}/L_{\rm star}$ selected sample. Instead, they are designed to probe systems with putative dust amounts below those currently detectable from warm dust surveys. Such a distance-limited systematic survey, extending in many cases to the stellar habitable zones, will reveal the levels of zodiacal light present in circumstellar debris systems. Stars in this sample hosting radial velocity detected extrasolar planets will be of particular interest as high-priority targets to better understand the connections between prior known exoplanets and the circumstellar material.

5.2 *Circumstellar Debris Systems with Previously Imaged Edgeworth-Kuiper Belt Analog Region Disks*

The EKB regions of approximately two dozen circumstellar debris systems have been imaged to date (mostly with HST coronagraphy), all with starlight-scattering fractions suggesting massive amounts of dust in the outer parts of those systems compared to our solar system. We illustrate one such ring-like circumstellar debris system about the close-solar analog star HD 107146 (G2V; 27 pc; with an estimated age of ~80 to 200 Myr) in Fig. 3. Its massive well-revealed EKB-analog debris ring is

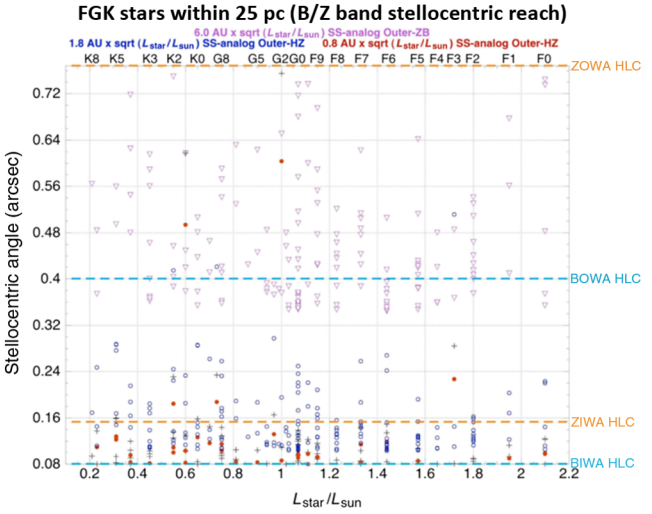

Fig. 2 Nearby stars with zodiacal-belt analog regions accessible to WFIRST CGI HLC.

Table 1 Currently conceived WFIRST CGI masks and spectral filters for disk imaging.

	λ/d		B (465 nm)		Z (890 nm)		Overlap B / Z
	IWA	OWA	IWA (arcsec)	OWA (arcsec)	IWA (arcsec)	OWA (arcsec)	resels
HLC	2.0	10.0	0.080	0.400	0.153	0.765	5.1/2.6
SPC	2.7	9.1	0.108	0.364	0.207	0.696	3.3/1.7
SPC/disk mask	6.5	24	0.250	0.959	0.497	1.836	9.5/5.0

2000× brighter in $f_{\rm disk}/f_{\rm star}$ than our solar system's seen with a comparable viewing geometry. Even for this dusty system, the HST coronagraphic mask at 0.44 arcsec is about twice the outer distance of its zodiacal-analog disk region beyond the edge, and the region is contrast-limited at 10^{-3} resel^{-1}.

Two of the currently known light-scattering circumstellar debris systems in this legacy sample, β Pictoris and Fomalhaut, have co-orbiting planets that have been revealed by imaging. For the case of β Pictoris, the planet orbits the parent star at ~8 AU, which is within the stellar-luminosity scaled outer zodiacal-belt analog radius. This massive debris system, however, bears little resemblance to the solar system (e.g., for holistic views of the β Pic system[16]), and some of its details are self-obscured due to its edge-on viewing geometry. The architectures of the zodiacal-belt analog regions of this otherwise well-studied legacy sample of circumstellar debris system remain unknown and ripe for exploration with WFIRST or EXO-C CGI imaging.

5.3 *Light-Scattering Circumstellar Debris System Candidates Detected at Longer Wavelengths*

Most light-scattering circumstellar debris systems imaged to date were originally identified from IRAS measured $L_{\rm IR}/L_{\rm star}$ excesses. Subsequent observations with improved sensitivities and for dust of different temperatures have suggested new circumstellar debris system targets. Some of the cold EKB-region dust structures (i.e., detected with Spitzer/MIPS ~5×10^{-6} and Herschel/PACS ~1×10^{-6}, $L_{\rm IR}/L_{\rm star}$ sensitivity limits) have been spatially resolved at thermal IR wavelengths.[17]

Until recently, the inner ~20 AU of many IR-identified circumstellar debris systems was thought to be relatively devoid of dust. However, it is now known from near-IR interferometric[18,19] and mid-IR photometric detections[20,21] that at least some circumstellar debris systems possess dust in close proximity to their central stars.[22–25] Indeed, there is growing evidence from IR photometry for multiple belts of interplanetary dust inside the planetary zones.[26] The origin of this terrestrial temperature dust is uncertain, though the rapid dust depletion timescales at these orbital distances imply that such particles must be transient in nature.[21] Warm zodiacal-analog disk dust, detectable with the Spitzer/IRS and Keck Interferometer (both with ~10^{-4} $L_{\rm IR}/L_{\rm star}$ sensitivity limits, and the soon-anticipated two-orders-of-magnitude improved sensitivity with large binocular telescope interferometer), is not yet detectable in scattered light, but would be with a WFIRST CGI.

Downloaded From: http://astronomicaltelescopes.spiedigitallibrary.org/ on 01/14/2017 Terms of Use: http://spiedigitallibrary.org/ss/termsofuse.aspx

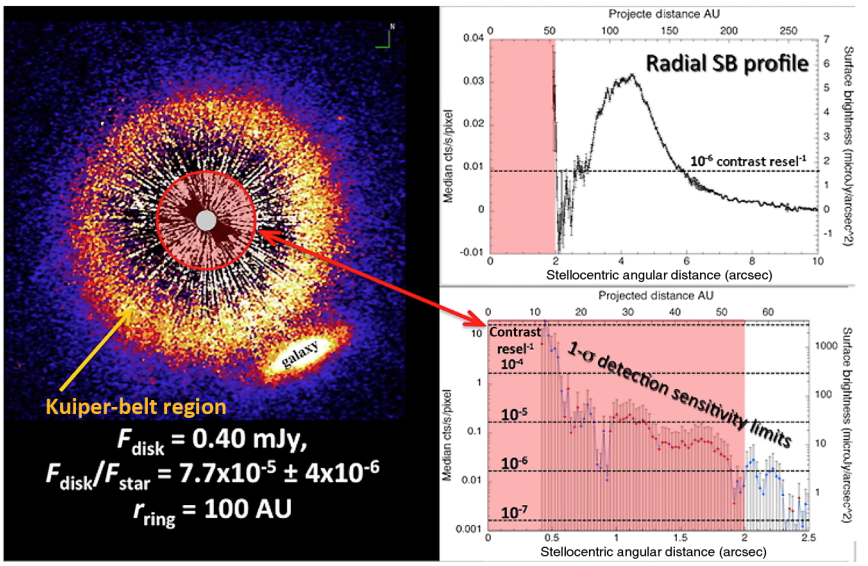

Fig. 3 HST visible scattered-light image of the HD 107146 EKB-analog region debris ring and instrumental limits precluding dust detection in the interior part of the circumstellar debris system (adapted from Ref. 1).

6 Contrast-Limited Detectability of Spatially Resolved Scattered-Light Disks

The detectability of exoplanets against the glare of their host stars is contrast-limited by the ability of any instrumental starlight suppression system to stabilize, reduce, characterize, and calibrate the intensity of instrumentally scattered and diffracted starlight in the stellocentric regions of interest. The instrumental inner-to-outer working angle range and corresponding azimuthally averaged stellocentric planet-to-starlight contrast ratio goals and requirements, enabled by a $\leq 10^{-9}$ contrast subarcsecond CGI, have been driven with priority for direct detection and characterization of exoplanets into the habitable zones of nearby stars.

A solar system zodiacal debris analog, with material orbiting within a few AU of the host star, observed at a distance of ~10 pc from the Earth, would appear within a stellocentric annulus of outer radius ~0.6 arcsec. This is within the CGI high-contrast stellocentric field (see Table 1). The requisite image contrast of $\sim 10^{-9}$ pixel^{-1} at stellocentric angles of ~0.1 to 1.0 arcsec at visible wavelengths with Nyquist or better pixel sampling is also immediately applicable and is particularly germane for uniquely characterizing circumstellar planet-hosting environments.

Detection sensitivity metrics for exoplanets in the contrast-limited domain are appropriately expressed for spatially unresolved point sources where most of the planet light is contained within a single pixel or diffraction-limited resolution element (resel). Discrimination between residual CGI-induced point-like optical artifacts and real planets by various methods may disambiguate these signals, which present themselves on similar, if not identical, spatial scales. Unlike planets, circumstellar debris systems are spatially resolvable at visible wavelengths by a WFIRST (or EXO probe) telescope. In many cases, circumstellar debris systems are anticipated to completely fill the high-contrast wavefront error–controlled field of view with potentially observable structures and substructures that inform the distribution and properties of light-scattering material in their inner zodiacal-belt analog regions.

For circumstellar debris systems, the area-integrated flux density of the starlight scattered by the disk particles into the observer's line of sight, $f_{\rm disk}$, is a measurable quantity analogous to the total planet light. This differs in circumstellar debris systems, however, in being spatially distributed over a large area, often with morphological complexity attributable to both the underlying physical processes responsible for sculpting the circumstellar dust and the viewing geometry. Nevertheless, the global ratio of the total disk light to that of its host star, $f_{\rm disk}/f_{\rm star}$ (i.e., the total dust scattering fraction), is a useful order-of-magnitude metric to gauge the overall relative brightness and potential detectability of circumstellar debris systems. However, the contrast-limited detectability of azimuthally and radially localized debris structures and substructures on various correlated spatial scales depends upon the surface brightness distribution of the light-scattering dust. For the approximately two dozen circumstellar debris systems thus far observed, this can vary by orders of magnitude spatially within any circumstellar debris system, or from one system to another, even if compensated for the r^{-2} falloff of the stellar radiation field in the plane of the disk. Viewing geometry alone (e.g., face-on versus edge-on) can result in order-of-magnitude differences in both $f_{\rm disk}/f_{\rm star}$ and localized surface brightness in structured disks, but details of dust density distributions can be responsible for larger dispersions in localized surface brightness and image contrast resel^{-1}.

6.1 *WFIRST CGI Stellocentric High-Contrast Field*

Herein we assume a WFIRST CGI high-contrast stellocentric field with raw image contrasts of $\sim 10^{-8}$ at a stellocentric angular distance of $\sim 4\,\lambda/D$ ($D = 2.4$ m) and $\geq \times 10$ contrast improvement through PSF postprocessing by speckle calibration or other methods. Similar or better contrast performance is expected for EXO-C. The WFIRST hybrid Lyot coronagraph (HLC) and shaped pupil coronagraph (SPC) designs have similar wavelength-dependent inner-to-outer working angle ranges (see Table 1, with a recently conceived larger disk mask under consideration) and resel^{-1} image contrasts, as shown in Fig. 1

Downloaded From: http://astronomicaltelescopes.spiedigitallibrary.org/ on 01/14/2017 Terms of Use: http://spiedigitallibrary.org/ss/termsofuse.aspx

(scaled to the extrema of the wavelength range for filter band imaging or exoplanet IFU spectroscopy).

6.2 *Coronagraphic Instrument Spectral Filters for Disk Imaging*

For disk imaging, we consider a minimum of two filter bands near the blue and red extremes of the CGI spectral range to provide a factor of $\sim\times 2$ in wavelength for maximum leverage to ascertain a visible color index for constraining particle properties.

The visible color sampled over the CGI wavelength range associated with particle types includes

1. large silicate particles that are neutral reflectors of stellar light;
2. organic-rich particles, such as those apparently observed in the HR 4796A disk,[3] which are red and would be ~50% fainter at 400 to 500 nm than at 800 to 900 nm;
3. only very small particles, such as those recently produced in high-velocity collisions, that produce a blue, Rayleigh scattering-like signature.

For representative dependencies of disk absorption and scattering efficiencies, and directionally preferential scattering phase function asymmetry factors (as well as degree of polarization) over the CGI ~2× wavelength range, see Fig. 11.

Here we consider a B filter with $\lambda_{\text{central}} = 465$ nm and a Z filter with $\lambda_{\text{central}} = 890$ nm, both with spectral bandwidths = FWHM (nm)/λ_{central} of ~10 to 20%. The central wavelengths are not critical, as they are not designed to match up with diagnostic spectral features (e.g., absorption bands that are largely absent at visible wavelengths). Strong intraband visible color gradients with spectral bandwidths <20% are not expected, so narrower bandwidth filters for spectral color diagnosis are unnecessary, and broadband spectral bandwidths of 10 to 20% provide greater sensitivity to dust-scattered continuum starlight. These particular bands satisfy the $\sim\times 2$ wavelength range criterion and are commensurate with the F465W and F890W filters proposed for exoplanet imaging with similar bandwidths (the latter used in conjunction with the IFU for exoplanet studies).

The B filter band provides the highest spatial resolution (e.g., 1 resel = 0.49 AU at 10 pc), critical to resolving and mapping disk substructures and asymmetries indicative of dynamical interactions with (possibly unseen) exoplanets. The B filter band also provides the smallest inner working distances (e.g., ~0.8 AU at 10 pc with the HLC), key to reaching into the inner parts of solar system analog zodiacal disks and stellar habitable zones. The Z filter provides the largest outer working angle (OWA), reaching in many cases beyond the outer regions of solar system analog zodiacal disks (e.g., 7.6 AU at 10 pc with WFIRST HLC, or ~18 AU at 10 pc for a conceptualized SPC disk mask).

The inner-to-outer working angle range of the CGI will scale with wavelength. The stellocentric angular ranges of overlap in B and Z band resels is from the Z (IWA) to the B (OWA), and will enable the search for color-differentiated particle sizes and properties. For a face-on disk, this probes a small but useful stellocentric annular zone. The physical range in stellocentric distance (AU) will increase for disks seen at higher inclinations—most usefully for disks seen at intermediate inclinations between face-on and edge-on viewing orientations. Importantly, the SPC is evaluating a larger IWA-to-OWA disk mask that could be extremely valuable to push further out in stellocentric angle to the inner regions of EKB-analog disks circumstellar debris systems.

7 Representative Disk Image Simulations with a WFIRST CGI

In this section, we present results from debris disk image simulations for a WFIRST CGI using an SPC with an image plane mask providing an IWA of $4.0\,\lambda/D$ and OWA of $12.4\,\lambda/D$ [corresponding to 187 to 583 milliarcseconds (mas) 550 nm]. This wedge mask differs in working angle extrema from the current Table 1 baseline and provides only an azimuthally restricted ≈56 deg bow-tie dark zone; it was adopted for simulations in this study for the timely availability of performance and related reference/calibration data with a 360-deg field synthesized by replication. These scattered-light image simulations are at a central wavelength of 550 nm with a spectral bandwidth = 10%; a broader filter (suggested up to spectral bandwidth of ~20%) would image disks more efficiently. The simulated images oversample the 550 nm PSF with 14.4 mas square pixels (i.e., 3.3 pixels per λ/D at 550 nm). Noiseless disk models are generated using the ZODIPIC IDL code (Kuchner and Stark, private communication[27]) assuming $T_{\text{dust}} \approx r^{-\Delta} \times {L_{\text{star}}}^{-\Delta/2}$ and $\Delta = 0.467$ (from the DIRBE model[28]). The noiseless disk models, including a scattered-light optical phase function from Ref. 29, are convolved with the SPC PSF for the same filter band (see Sec. 7.5). The raw stellocentric contrast field (speckle file provided by Krist[30]) is attenuated by ×10 as a presumed minimum planned/achievable with speckle calibration (subtraction) in postprocessing. Photon noise from both the disk and the raw (unattenuated) speckles are added with integration time of 10 h. An end-to-end system throughput efficiency of 35% is assumed.

7.1 *Dynamically Featureless Disk—10-h Visit on a Close-Solar Analog*

The first of these simulated images, shown in Fig. 4, is for a hypothetical solar system–like, optically thin dust disk circumscribing the planet-hosting star 47 Uma (G1V; 14.2 pc; $V = 5.04$; age ~6 Gy[31]), but with no model planets implanted. The model disk has 30 zodis of solar system–like dust with a power law particle density distribution $\propto (r/r_0)^{-\alpha}$ with $\alpha = 1.34$ as suggested by the DIRBE model of our Solar System.[28] One zodi of dust has a face-on optical depth of $7.1 \times 10^{-8}\, r^{-0.34}$ (where r is the stellocentric distance in AU) and corresponds to the amount of dust in our solar system. The disk is featureless in that it exhibits no central clearing (e.g., by planets or dust sublimation exterior to the IWA limits of the coronagraphic mask at 2.7 AU), with no deviations from a continuous radial power-law profile nor azimuthal asymmetries that might arise from co-orbiting planets. The disk is viewed with a sky-plane projected inclination of 60 deg from face-on resulting in an $r^{-2.27}$ power-law index surface brightness distribution along the disk major axis. The major axis of the disk is oriented 45 deg with respect to the detector x/y pixel grid.

This single image (1) detects the disk with ~6 to $15\,\sigma$ resel^{-1} along the disk major axis, which then (2) closely recovers the disk global morphology and extent, (3) enables a quantitative determination of the major axis radial surface brightness profile as $r^{-1.97}$ (see Fig. 5) in rough agreement with the model image

Downloaded From: http://astronomicaltelescopes.spiedigitallibrary.org/ on 01/14/2017 Terms of Use: http://spiedigitallibrary.org/ss/termsofuse.aspx

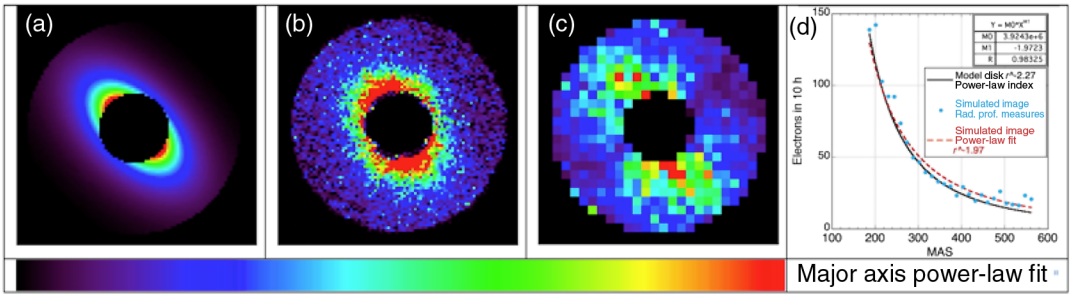

Fig. 4 (a) Noiseless, 550 nm, 47 UMa 30 zodi disk model at CGI pixel scale with flux density (linear color encoded scale bar): 1×10^{-10} Jy to 5×10^{-9} Jy pixel^{-1}. (b) Simulated SPC image including residual speckles and photon noise with 10 h integration time, 0 to 115 photons pixel^{-1}. (c) Per resolution element SNR map: 1 to 15. (d) Estimation of the disk major axis power-law index best fit from its measured surface brightness profile.

(power-law index ± 0.3, invertible to surface density with similar uncertainty), and (4) is devoid of image artifacts that could be misinterpreted as planet-presence or radial differentiation in particle properties.

7.2 *Multiple Roll Observations—Recommended Strategy for Disk Characterization*

The residual stellocentric contrast field (i.e., speckles) is rotationally invariant at the detector image plane, assuming a thermally stable environment. To the extent that the residual speckles are stable with observations at two or more spacecraft roll angles, the speckle structure in coregistered target images will stochastically decorrelate with coaddition in a common celestial frame. This further improves disk detectability, recovery of astrophysical image structure, and overall image fidelity. This approach has been highly successful with space-based visible coronagraphic imaging of the outer EKB regions of circumstellar debris systems accessible with HST and is equally applicable to the more demanding combined contrast and IWA delivered by a WFIRST CGI.

In Fig. 5, we illustrate a three-roll observation of the same 47 Uma hypothetical disk considered in Sec. 7.1, but observed at three orientation angles with respect to the CGI frame differing from the prior position angle by ± 15 deg. (For illustration, we assume a spacecraft off-nominal roll capability of ± 15 deg. Any differential roll capability sufficiently large to rotationally decorrelate image artifact structures on the spatial scale of the speckles at the IWA will suffice for this purpose.) The individual 10-h simulated exposures are shown at the bottom of Fig. 5 with disk major axis position $\times$ angles $= 30$ deg [Fig. 5(a)], 45 deg [Fig. 5(b)], and 60 deg counterclockwise [CCW, Fig. 5(c)] from vertical in the CGI frame. All three images are then rotated to a common [Fig. 5(b)] celestial frame. With differential rotation, the speckle pattern partially decorrelates, providing a spatially smoother background when coadded [Fig. 5(d), top], as evidenced in the higher fidelity disk image [Fig. 5(d), bottom].

N-roll observations are N times more expensive than spacecraft time-on-target; for example, in this case, consuming 30 h (with $N = 3$) to obtain the final image in Fig. 6(d). An added benefit of this multiroll observing strategy is also a root(N) improvement in photon signal-to-noise ratio (SNR), separate

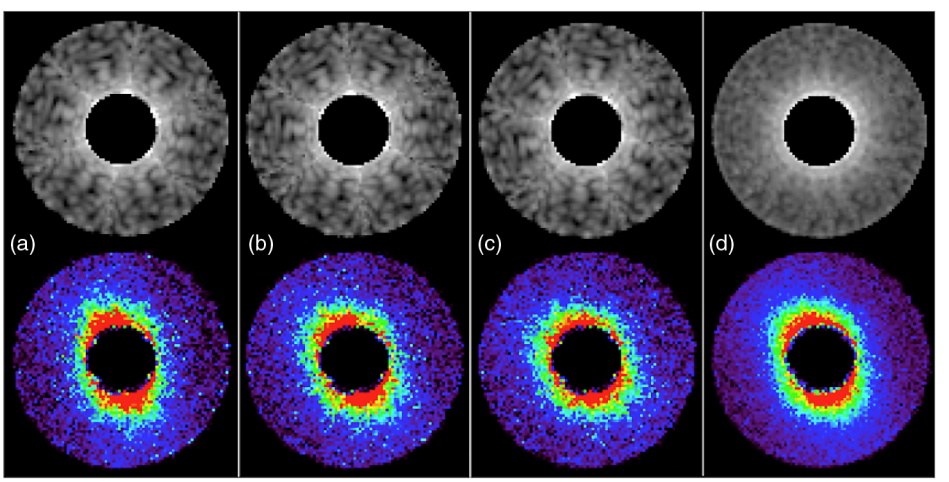

Fig. 5 (a) through (c) First row: the underlying SPC 56 deg wedge mask speckle pattern (synthesized circumferentially over a 360 deg field by replication) after rotating the disk images (a) and (c) by $+15/-15$ deg CCW to a common celestial orientation, which is then averaged in (d). Shown is a $\log_{10}$ stretch (to best illustrate speckle structure) from 1 (black) to 100 photons (white) pixel^{-1} without photon noise for illustrative purposes. Second row of (a) through (c) shows individual 10-h CGI frame simulated exposures, as in Fig. 4 [for (b) identically] with the disk at 30, 45, and 60 deg CCW (before rotation), which is then combined (averaged) in (d) after co-rotation to a common celestial frame. Same color stretch as in Fig. 4.

Downloaded From: http://astronomicaltelescopes.spiedigitallibrary.org/ on 01/14/2017 Terms of Use: http://spiedigitallibrary.org/ss/termsofuse.aspx

from decorrelating the residual speckle structure. N-roll observations should be considered at the outset for high-priority circumstellar debris system targets, or as a follow-up to improve upon observations of newly discovered zodiacal disk analogs from $N = 1$ survey observations.

7.3 *Exoplanetary Zodiacal Debris Ring: Evidence for and Constraining Planet Presence*

A second disk simulation is for a nearby star of particular interest, Epsilon Eridani (K2V; 3.4 pc; $V = 3.73$; age ~850 Myr), which possesses an ~35 to 75 AU radius EKB debris ring that is spatially resolved (and clumpy) at 850 μm. This disk, with peak emission at 60 AU (=18 arcsec due to its close proximity to Earth), is (yet) undetected in scattered light and is estimated to contain $\sim 1/6\, m_{\rm lunar}$ of debris dust. Spitzer observations suggest two belts of warm dust orbiting closer to the star as modeled by Backman et al.[26] at stellocentric distances of ~20 AU ($\Delta r/D = 0.05$) and ~3 AU ($\Delta r/D = 0.17$), with optical depth and mass density scaling with ratio of an annular debris ring's width (Δr = inner to outer edge distance) to its stellocentric diameter (D). The detected presence of such a ring and the sharpness of its edge profiles revealed by spatially resolved imaging puts dynamical constraints on the existence of co-orbiting planets, their orbits, and masses, and on the locations of parent bodies responsible for the light-scattering dust.[32]

Epsilon Eridani has a radial velocity detected exoplanet candidate with an astrometrically determined mass of $1.55 \pm 0.24\, M_{\rm jup}$ and orbital semimajor axis of 3.39 AU.[33] A second unconfirmed planet has been suggested with ~40 AU, and Backman et al.[26] comment that the circumstellar disk architecture, suggested from modeling IR to millimeter wavelength observations, may require three planets.

Here we test the ability of a WFIRST CGI to detect and resolve a posited centrally cleared ring-like zodiacal belt. The architecture of an Epsilon Eridani planetary system is not well established, nor is it known how additional inner planets (if any) may actually affect an inner zodiacal belt dust distribution. With those caveats, we place a hypothetical ring midway between the suspected $1.55\, M_{\rm jup}$ planet's semimajor axis and the star, with an architecture suggested by and scaled from our solar system's main asteroid belt; this model has an inner edge at 1.4 AU, outer edge at 2.28 AU, and maximum dust density at 1.75 AU. We consider total dust masses equivalent to both 30 and 100 zodis and particles with an albedo of 0.17 that scatter isotropically. We assume no other dust components, nor the planet itself, in these image simulations. While an inner planetary system need not be coplanar with the outer EKB ring that is inclined 65 deg from face-on, that inclination is in good agreement with that of the putative Epsilon Eridani planet,[33] and we adopt this inclination also for this zodiacal disk image simulation.

The instrumental configuration (SPC, IWA/OWA, filter band, and bandwidth) is identical to the earlier presented disk simulation for 47 Uma (Sec. 7.1). Here, too, we separately integrate for 10 h in each of the three celestial orientations of the astronomical field off-rolled by −15, 0 (nominal), and +15 deg, with nominal arbitrarily at a disk major axis orientation of 45 deg with respect to the detector x and y focal plane. Results are shown in Fig. 6. The debris ring is clearly detected and well resolved in each of the three off-rolled images [Figs. 6(a), 6(b), and 6(c) with 30 zodis of dust mass, and with better clarity in Figs. 6(f), 6(g), and 6(h) with 100 zodis], and its centrally cleared architecture is unambiguously revealed along with its morphology and geometry. Any one of these single images would serve well in a discovery mode survey and provide a preliminary characterization of the zodiacal ring architecture and photometry. Combining the three images for each case separately into a common celestial frame [Fig. 6(d) or 6(i)] both improves the fidelity of the disk image by partial decorrelation of the residual speckle structure and enables photometry with peak SNR resel^{-1} at the ring ansae of ~15 and 40 [Figs. 6(e) and 6(j), respectively].

For the 100-zodi case, in Fig. 6, we compare the noiseless debris ring model (top left) to the three-roll combined simulated image [bottom left, identical to Fig. 6(i), but rotated to put the disk major axis on the image horizontal]. A three-pixel (averaged) wide, IWA-masked radial profile cut along the disk major axis centered on the location of the star is shown for the CGI-simulated image in comparison to the disk model. Inwardly increasing residual light from the star dominates the inwardly declining disk surface brightness at $r < 375$ mas. At larger stellocentric angular distances, the radial structure of

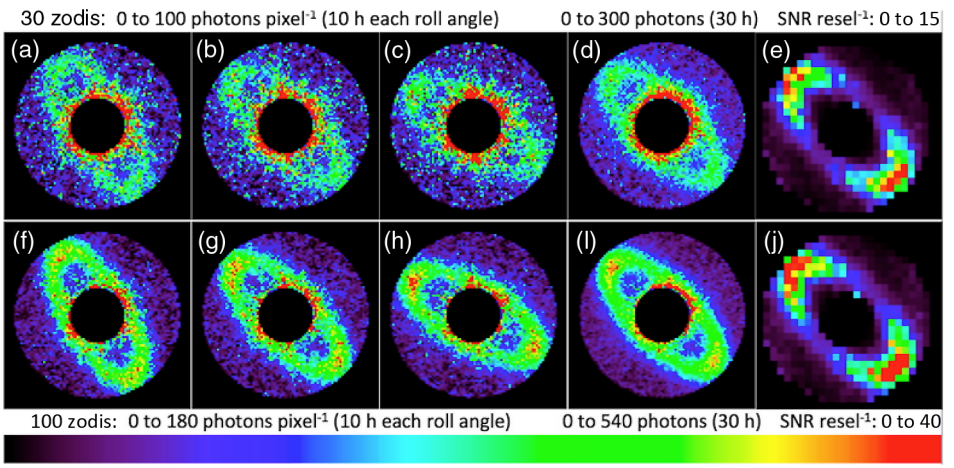

Fig. 6 Disk image simulations for hypothetical 30- (first row) and 100- (second row) zodi inner debris rings circumscribing ε Eri at $r = 1.75$ AU. Left three panels (each) differentially oriented on the sky by −15, 0, and +15 deg. (d) and (i) Each combines the corresponding three off-rolled images with resulting SNR resel^{-1} maps indicated in (e) and (j).

Downloaded From: http://astronomicaltelescopes.spiedigitallibrary.org/ on 01/14/2017 Terms of Use: http://spiedigitallibrary.org/ss/termsofuse.aspx

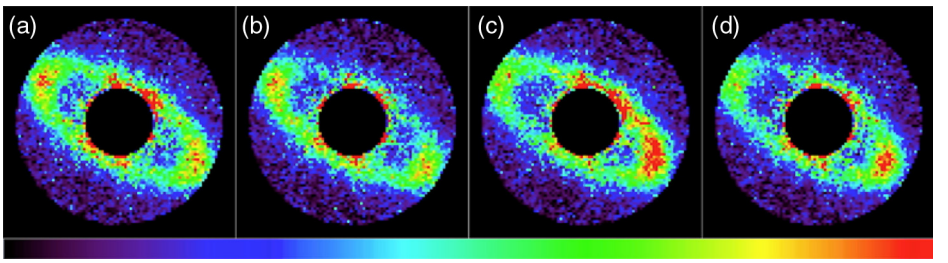

Fig. 7 WFIRST CGI-simulated 10-h surface brightness images (0 to 180 photons pixel^{-1} linear dynamic range in all panels) of a 100-zodi debris ring per Sec. 7.2 formulation. (a) As shown previously, with isotropic scattering, SNR resel^{-1} ~ 15 at the ring ansae, (b) with a nonisotropic scattering phase function (φ) per Ref. 29 with a three-component Henyey-Greenstein linear superposition prescription, (c) isotropic scattering but with an 11% ring stellocentric offset from the central star with pericenter at $\theta = 335$ deg (CCW from image vertical) in the ring plane, (d) simultaneously the same nonisotropic scattering as in (b) and the pericentric offset as in (c). The imaged surface brightness asymmetries discriminate between possibilities.

the debris ring is recovered with high fidelity, though broadened at $r \leq r_{peak}$.

In particular, with an SNR of ~20 to 40 resel^{-1} [Fig. 6(j)] from the half-power points across the ring ansa, (1) the surface brightness peak locations are precisely recovered; (2) Δr is increased by only 4% of D (39.5 mas for this case), primarily as a consequence of the stray light interior to the ring peaks, but also in lesser part in convolution with instrumental PSF (see Sec. 7.5 and relevant discussion vis-à-vis the morphologically similar HR 4796A debris ring by Schneider et al.[1,3]); and (3) the ring-edge slopes are closely preserved. Items (1) through (3) together provide a high-fidelity tracer of planet presence, orbital chaotic exclusion zone location, and planet mass characterized by the ring semimajor axis.[34]

7.4 *Pericentric Offsets and Nonisotropic Scattering Phase Functions*

The presence of a (massive) planet can perturb otherwise stellocentric dust particle orbits, resulting in a pericentrically offset debris ring.[35] A pericentric offset will not only displace a debris ring center but also result in diametrically opposed Δr^{-2} surface brightness asymmetries in the disk plane from particles closer to and further from the star.

Light scattered by circumstellar particles may have directionally preferential scattering phase angles with dependencies on particle sizes (compared to the observational wavelength) and properties that can be betrayed (or constrained) by azimuthal surface brightness variations in the projected plane of the disk (to the line of sight of the observer), i.e., with scattering phase angle of ($\varphi = \cos^{-1}[\sin(i)\cos(\theta)]$, with i = inclination and θ = disk-plane azimuth angle; see, e.g., Ref. 36). The surface brightness dependence of φ is unexplored with face-on disks and is fully explored for edge-on disks, but is conflated in the latter case by the increased optical depth and quadrant degeneracy through the dust along the edge-on line of sight. Intermediate inclination disks are the best targets for modeling and interpretation of observationally derived φ.

Figure 7 illustrates the WFIRST CGI sensitivity to both pericentric offsets and nonisotropic φ for a hypothetical 100-zodi Epsilon Eridani zodiacal belt per Sec. 7.2 with single 10-h exposures. Figure 7(a) is for an isotropically scattering debris ring with no pericentric offset [as shown prior in Fig. 6(g)]. In Fig. 7(b), we introduce and recover a[29] φ, appropriate at $\lambda < 4$ μm, with a strong front-to-back asymmetry in scattering efficiency with φ. Such a strong asymmetry is seen in polarized light (only) for the HR 4796A debris ring. In Fig. 7(c), with

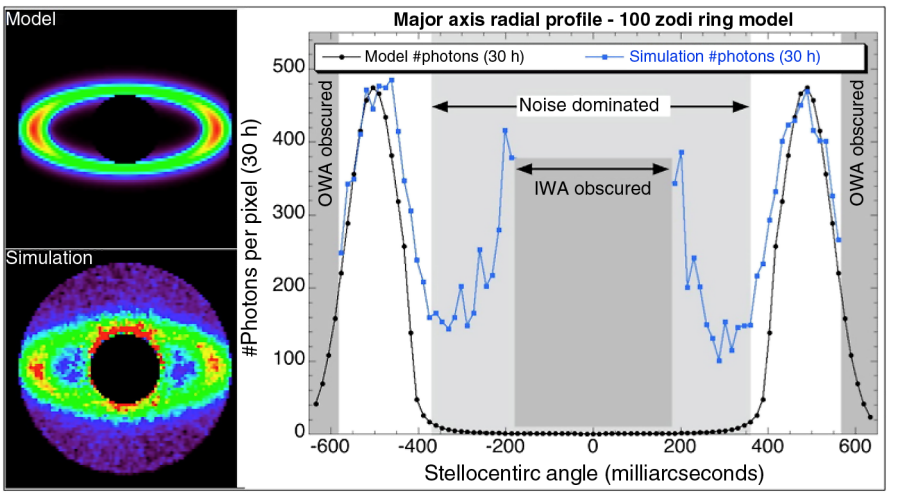

Fig. 8 Comparison of noiseless model and CGI simulation of the 100-zodi debris ring scattered-light images with per-pixel radial surface brightness profiles along the disk major axis. The region marked "Noise dominated" is the region dominated by residual noise, both systematic and photon. The OWA of the CGI simulation with the SPC mask obscures the ansa part of the ring at $r > 583$ mas, beyond the FWHM$_{outer}$ = 569 mas radius of the simulated ring peak surface brightness.

Downloaded From: http://astronomicaltelescopes.spiedigitallibrary.org/ on 01/14/2017 Terms of Use: http://spiedigitallibrary.org/ss/termsofuse.aspx

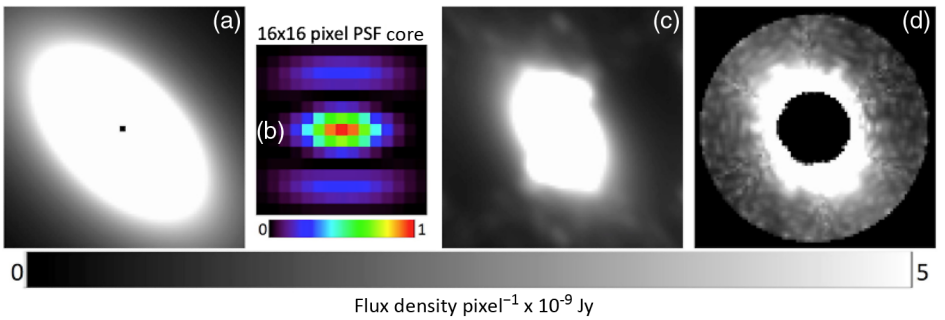

Fig. 9 (a) Model disk, (b) SPC/wedge-mask PSF core region unity normalized to central pixel brightness, (c) model convolved with the full PSF, and (d) convolved model with residual speckles. (a) and (c) shown beyond the image-plane mask imposed IWA/OWA.

isotropic scattering, we introduce a disk-plane stellocentric offset of 11% ring radius with the pericenter 45 deg clockwise (CW) from the projected ring's upper semiminor axis. Both the r^{-2} pericentric glow and the ring's astrometric decentering are recoverable from the image. In Fig. 7(d), we apply both the nonisotropic φ and the pericentric offset in addition to the still-obvious (OWA-limited) astrometric offsets of the ansas. This produces, in combination, a morphological intra-ring gap that is more pronounced with bilateral asymmetry on the back side of the ring.

Note that the Hong formulation is a Henyey-Greenstein φ representation using a linear combination of φ asymmetry parameters, g_n, for solar system zodiacal dust. We do not suggest this is the best representation, but use it for demonstration. Recent analysis of scattered-light imaging of the HD 181327 circumstellar debris system[37] with a single Henyey-Greenstein asymmetry parameter for its debris ring fails to reproduce the observed surface brightness distribution over the full φ range. In that case, a two-component model with $g_1 = 0.87$ and $g_2 = -0.30$ weighted 86 and 13%, respectively, is much better—with possible implications for two discrete populations of dominant particles in the debris birth ring.

7.5 *Point Spread Function Convolution (/Deconvolution)*

The complex structure of a spatially variable or asymmetric PSF (e.g., WFIRST HLC or SPC, respectively) in convolution with the true spatially resolved astronomical scene can

1. broaden spatially resolved features (e.g., narrow- or sharp-edged rings, gaps, clumps, and other substructures);
2. distort the two-dimensional morphology of the disk (as in Figs. 6 and 8);
3. result in flux loss within the stellocentric working angle limits of the image plane mask.

We comment on each of these below.

1. The two-dimensional structure of the WFIRST HLC PSF is field-point dependent. Thus, full recovery of the detailed morphology of a spatially resolved source (i.e., circumstellar disk) with high precision may require anamorphic or other field-dependent PSF deconvolution/reconstruction techniques, but may be difficult, if not problematic, at a low SNR.
2. Convolution distortion is the reason for the apparent CW rotation (skew) of the disk major axis orientation in the SPC simulated images in Figs. 5 and 6 compared to the noiseless model in Fig. 8. This effect is illustrated in Fig. 9, which shows the noiseless morphology of that model disk (with the central star removed) before [Fig. 9(a)] and after [Fig. 9(c)], and PSF convolution with the WFIRST SPC PSF [Fig. 9(b) showing its central region] and 56-deg wedge mask. In Fig. 9(d), the wedge-mask contrast field (speckles

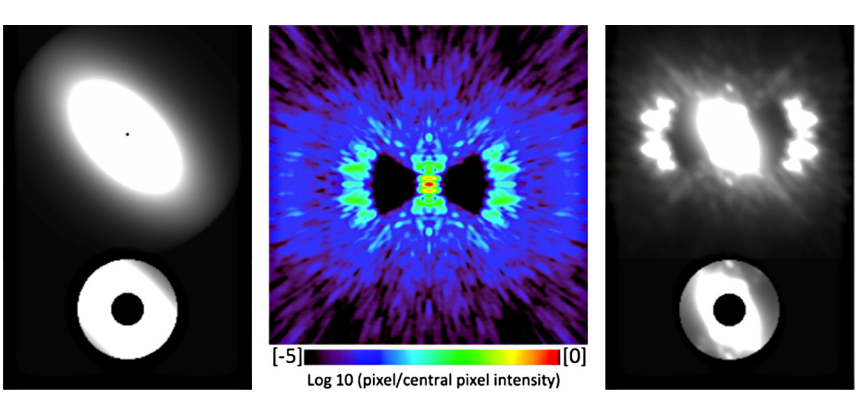

Fig. 10 Noiseless disk model (left) in convolution (right) with the "full" (256 × 256 pixel = 3.7 × 3.7 arcsec) SPC PSF (middle); bottom of each with the SPC field stop. Middle: PSF with $\log_{10}$ stretch normalized to the central pixel brightness. Pixels in green beyond the OWA periphery of the wedge-mask are suppressed by only ~0.3% of the central pixel intensity with flux redistributed/enhanced beyond the SPC OWA in the convolved (right panel) image.

Downloaded From: http://astronomicaltelescopes.spiedigitallibrary.org/ on 01/14/2017 Terms of Use: http://spiedigitallibrary.org/ss/termsofuse.aspx

with postprocessed ×10 attenuation) has been added, tiling a full 360 deg in simulation by abutted sector replication. This is the same image as in Fig. 4 but without (for illustrative purposes) the addition of photon noise.

This distortion effect could be mitigated with a more symmetrical PSF (e.g., HLC, but note its field dependence), or potentially with differentially reconstructed modeling from multiroll observations. In the latter case, further study is required to ascertain the degree of calibratability in the general situation of an arbitrary (two-dimensional) disk surface brightness distribution.

3. Additionally, disk flux within the SPC FOV, with convolution, is not fully conserved and is therein underestimated overall [e.g., compare Figs. 10(a) and 10(d) shown in an identical linear stretch]. Flux from the disk is also redistributed in convolution exterior to the SPC OWA (e.g., Fig. 6, top right). Beyond the field stop is unimaged; hence, this flux is irrecoverable even with image-based deconvolution where an exquisite knowledge of the instrumental PSF exists.

8 Polarimetry of Circumstellar Debris Systems

Polarimetric optics are being considered for the WFIRST CGI, primarily for optimizing the contrast, and future EXO-C may also include such optics. It is therefore useful to explore polarimetry in relation to the study of debris disk systems. Imaging photometry alone, while highly informative in characterizing the distribution and physical properties of circumstellar material, is often not sufficiently constraining to arrive at nondegenerate answers to questions such as those posed in Sec. 2. Polarimetry, the additional piece of information that defines the full state of an electromagnetic wave scattered from circumstellar material (and planetary atmospheres and surfaces), though often ignored, can provide key information and insights to arbitrate between conflicting theories in otherwise observationally ambiguous domains. With wavelength dependence and measurement of the polarimetric state, degeneracies between material properties, optical constants, and disk viewing geometries can be broken. For detailed discussion, see Ref. 38.

8.1 *Characterizing Circumstellar Material with Two-Band Imaging Polarimetry*

Debris dust should represent the material being delivered to planet surfaces by asteroids, comets, and meteoroids in (exo) planetary systems. For an optically thin medium, such as the dust in a circumstellar debris system, spatially resolved measurements of the color, the degree of linear polarization (DoP), and the scattering phase angle of light scattered into our line of sight will strongly constrain the particle size, composition, and porosity (e.g., Fig. 11). This, in turn, constrains the type of parent planetesimals (rubble pile or differentiated body) and its volatile (e.g., carbon and ice) content.

The DoP (also called the fractional linear polarization, p, or as a percentage $p\%$) of a polarized source is the polarized intensity normalized by the total intensity (I): $p = (Q^2 + U^2)^{1/2}/I$, derived from the full-linear Stokes components. The polarization position angle of the source $\theta = 1/2 \tan^{-1}(U/Q)$. Q and

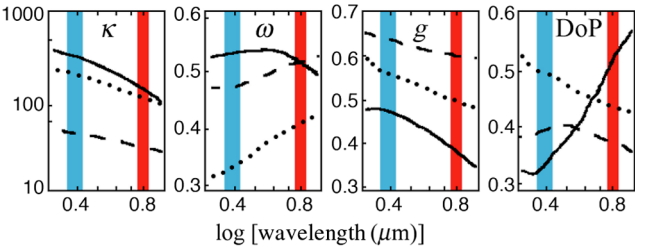

Fig. 11 Circumstellar polarization signals are scattering angle and wavelength dependent. Two-band polarimetric imaging observations can measure and further disambiguate debris dust properties, here shown over the ~2× CGI wavelength range. Disks may be full of volatile-rich porous particles that carry water and carbon to planet surfaces, or may be composed of compact and bone-dry spherules. Different particle types have different wavelength-dependent absorption (κ) and scattering (ω) efficiencies, directionally preferential scattering phase functions (isotropic: $g = 0$, complete forward scattering: $g = 1$ for Henyey-Greenstein scattering), and maximum DoP. Examples here compare compact particles like those in the interstellar medium (solid lines), moderately sized fluffy aggregates (dotted[39]), and larger particles inferred in some circumstellar disks (dashed[40]).

U are measured with a set of polarimetric analyzers with the absolute measurement of the total intensity in the same bandpass (e.g., see Ref. 41). With orthogonal-only polarization analysis (such as with ordinary/extraordinary ray splitting with a single Wollaston prism), only Q can be measured and $p\%$ cannot be determined; see Sec. 8.6).

These properties cannot be unambiguously determined from models of the IR-to-millimeter wavelength spectral energy distributions alone, because such models are degenerate between particle properties and disk radial structure (e.g., see Fig. 12). By spatially resolving the disk at two wavelengths and in DoP, such degeneracies can be broken (e.g., see Fig. 13).

For an optically thin ($\tau < 0.7$) scattering medium, the single-scattering (linear) polarization is a simple function of the scattering angle.

1. For a small vertical scale height and a thin ring of scatterers, the polarization is dominated by scattering angles near 90 deg for edge-on disks, so $p\%$ is ~30 to 40% or possibly higher.
2. As the inclination increases, the polarization fraction will still be high in regions with projected scattering angles of ~90 deg.
3. For a face-on disk, all scattering angles are 90 deg at any stellocentric azimuth angle.

A reason for historically reported decreased polarization in face-on disks is likely beam dilution from the projected angular size of the (seeing- or early AO-performance-limited) resel.

In cases (1) and (2), the maximum polarization fraction will be wavelength and particle size dependent (e.g., see Fig. 14).

All such particles polarize, but porous aggregates and absorbing particles, such as particles from icy comets, polarize more than compact particles produced in collisions of differentiated asteroids (e.g., Ref. 42). The DoP, as a function of wavelength, constrains the particle composition and size distribution. The DoP is also a strong function of scattering angle, from up to 100% for right-angle scattering by small particles to zero for forward or backward scattering. Thus, polarimetry is a powerful

Downloaded From: http://astronomicaltelescopes.spiedigitallibrary.org/ on 01/14/2017 Terms of Use: http://spiedigitallibrary.org/ss/termsofuse.aspx

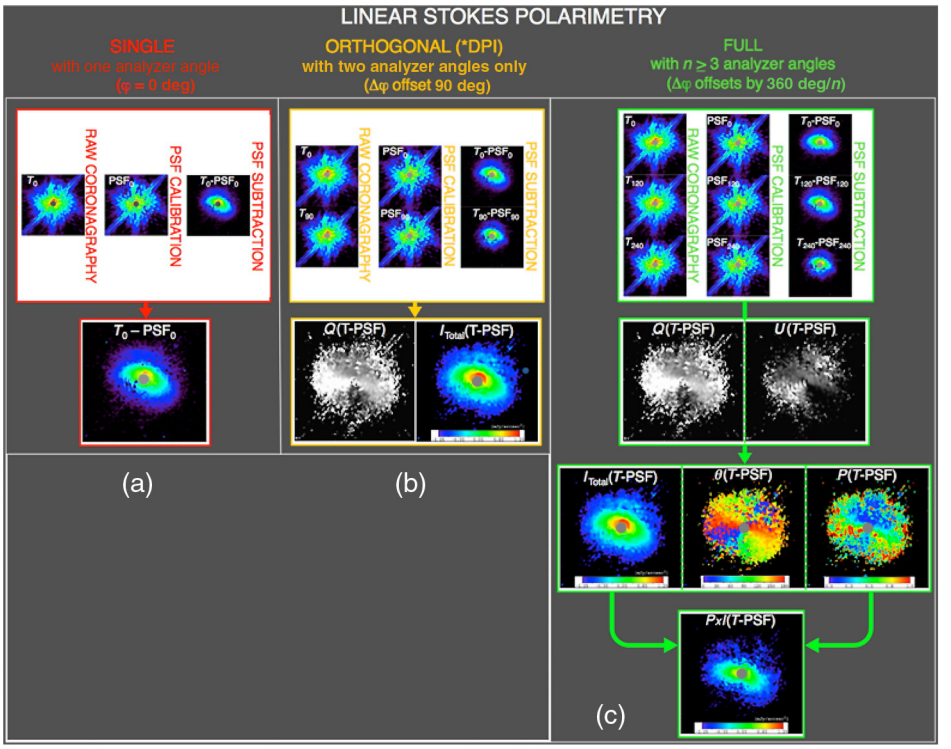

Fig. 12 Demonstration observations using HST/NICMOS 2.0 μm coronagraphic polarimetry of the GM Aur circumstellar disk with PSF calibration/subtraction for ×10 contrast augmentation (analogous to CGI speckle calibration). The information derivable from full-linear Stokes polarimetric analysis depends upon the number of proper analyzer angles employed. (a) A single polarizer ambiguates and dilutes intensity information, returning only the pseudovector component of the total intensity in the direction of the analysis axis angle. (b) Differential polarimetric imaging (DPI) with orthogonal polarimetric analyzers provides only the total intensity and Stokes Q, only informing on the presence of polarizing particles. (c) Full-linear Stokes polarimetry, in addition to providing Stokes Q and U, yields the total intensity (disk surface brightness), polarization fraction (p), and thus also the polarized intensity ($p * I$), as well as the electromagnetic field orientation on the sky (θ). Together these quantities provide strong constraints on the physical properties of the light-scattering/polarizing particles.

probe of disk structure, including vertical height distribution, inner-hole size, and inclination. For disks that are modestly inclined to the line of sight, the DoP as a function of azimuth angle and color places strong constraints on particle size and porosity as a function of position in the disk (e.g., Ref. 43). Particles in areas strongly perturbed by planets, and showing image structure may have different size distributions than those in quiescent locations.

Once the scattering and polarizing efficiency of disk particles are known, these can be combined with existing longer-wavelength data (e.g., from IRAS, Spitzer, Herschel, and WISE) to determine the particle absorption efficiency. Together, scattering and absorption efficiency yield the particle albedo, another measure of composition (e.g., see Fig. 5 in Ref. 24). This approach has been demonstrated successfully in modeling HST observations not only of the EKB-analog regions of circumstellar debris systems (HD 181327,[37] AU Mic,[44] HD 61005[32]), but also for protoplanetary disks around young and older classical T Tauri stars (e.g., GM Aurigae,[45] IM Lup[46]) and transitional disks around Herbig A/F stars (e.g., AB Aurigae[43]).

Identifying the presence of icy and organic-rich (absorbing) particles in disks will give the first clues to the presence of volatiles important for life. Spatially resolved imaging polarimetry is thus crucial to disentangling the dynamical and compositional history of disks.

8.2 *Polarimetry of Zodiacal Disks*

In Sec. 8.1, we discussed how the physical properties of circumstellar materials can be characterized with imaging polarimetry. These methods are equally valid and applicable to both the outer (EKB-analog) cold dust regions of circumstellar debris system where they have been applied (as exampled in Sec. 8.1) and, contiguously, into the inner (zodiacal-belt analog) warm dust regions yet unexplored in exoplanetary debris systems. Elucidating and constraining the material composition, particle geometry, size distributions, and degree of structural complexity (e.g., porosity) of circumstellar materials in combination, augmented with CGI-enabled spatially resolved polarimetry, is highly compelling, perhaps more so in the warm dust region uniquely explorable at CGI contrasts than in the fossilized relics that are the cold dust disks explored to date primarily with HST.

It is in the warm dust regions where terrestrial planets are posited to form, and where the systemic ice lines may be found, interior to which mantled volatiles otherwise found in the outer disks have sublimated off their circumstellar particles. One of the key conundrums in forming terrestrial planets in these dry zones is subsequently making them wet. Investigating circumstellar dust properties in zodiacal disks directly probes this environment, and spatially resolved imaging polarimetry can inform on the existence of ice lines in zodiacal

Downloaded From: http://astronomicaltelescopes.spiedigitallibrary.org/ on 01/14/2017 Terms of Use: http://spiedigitallibrary.org/ss/termsofuse.aspx

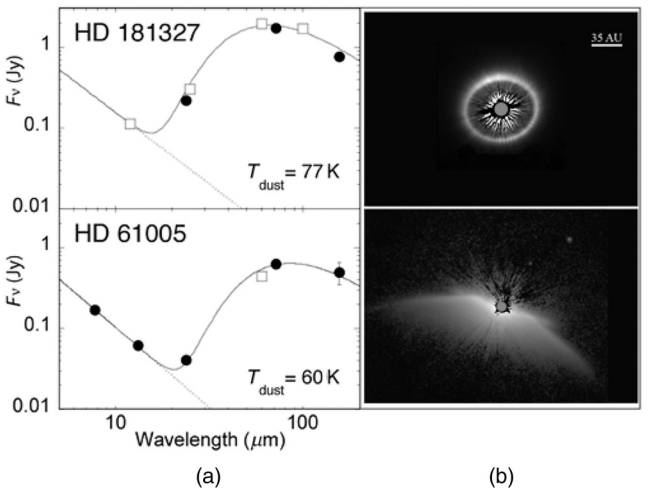

Fig. 13 (a) Disk geometries (in particular inclinations) and morphologies cannot be determined by thermal IR excess alone. Small particles radiate less efficiently than large particles. Therefore, at a given equilibrium temperature, small particles reside farther from their central stars than large particles. For example, IR-excesses measured by IRAS (squares) and Spitzer (dots) for the dominant particle populations around the circumstellar debris system hosting stars HD 181327 (top) and HD 61005 (bottom) indicate similar temperatures assuming emission from particles at a single stellocentric distance. Drastically different disk morphologies (and inclinations) are, however, revealed in (b) with scattered light imaging (HST/STIS[1]).

disks through telltale signatures of radial discontinuities in circumstellar particle polarizations. The dynamical history of the terrestrial planet formation in our own solar system is being deciphered by studying the composition of the main-belt asteroids and Centaurs, with one of the key puzzles—how did Mars form (e.g., see Ref. 47) in the context of the Grand Tack model of the early evolution of the inner solar system (Ref. 48)? We cannot measure asteroids and Centaur-like objects directly in exo-solar debris disks, but we can ascertain the dust particle properties from debris liberated by the collision of these parent objects, with the polarimetric sensitivity to low surface brightness dust.

8.3 *WFIRST CGI Polarimetric Analysis*

The baseline CGI technical design incorporates the use of a single fixed linear polarimetric analyzer to mitigate the deleterious effects from intrinsic intrapupil polarization mixing due to variation in beam angle from the primary mirror. In the currently envisioned implementation, this is done by using only one of two orthogonal polarization states produced by a Wollaston prism for the combined instrumental-plus-astrophysical signal of highest contrast. The other beam is captured, but not optimized for highest contrast. This technique may be required to reach a focal plane image contrast (target-uncorrelated starlight suppression) requirement.

This two-beam system can be used to obtain a second set of images optimized for the orthogonal beam, which, combined with the image(s) from the first beam, would yield one of the linear Stokes parameters (Q). By obtaining a second set of exposures at a different spacecraft roll angle, the second linear Stokes parameter (U) can be determined. Together, then, the polarization of the system can be derived.

Astrophysical linear polarization fractions (DoP, or $p\%$) of circumstellar debris system material and exoplanet atmospheres are not expected to be 100%, but are often likely to be on the order of tens of percents (e.g., Stam et al.[49] and Perrin et al.[43]). Detection of such a signal with observations using the current baseline WFIRST CGI should be possible.

8.4 *Full-Linear Stokes Polarimetry Implementation Architectures*

High-contrast (coronagraphic) full-linear Stokes imaging polarimetry is a capability that is not currently planned for future NASA astrophysics missions, but could be considered for an EXO-C CGI as a potentially low-cost value-added capability. A CGI full-linear Stokes polarimetery capability, integral to a starlight suppression system with wavefront error control to deliver high contrast, would enable exploration into zodiacal-belt analog regions of circumstellar debris systems.

Several different implementation strategies may be considered. A simple and spaceflight-tested method that has been used for the vast majority of modern dual-beam polarimeters

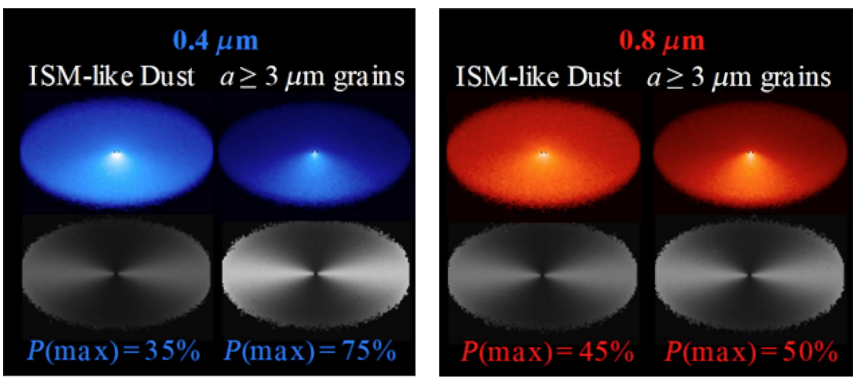

Fig. 14 Monte Carlo scattering models. Total intensity images for circumstellar disks with a surface density $\propto 1/r$ are shown in the first row. Larger particles show a stronger forward versus backward scattering asymmetry that is greater at shorter wavelengths. Polarization (DoP) maps of the same disks (grayscale; $p\% = 0\%$ black, $p\% = 100\%$ white) are shown in the second row. In both spectral bands, larger particles produce higher linear polarization, but large particles polarize light much more efficiently than smaller particles. Thus, two-band imaging polarimetry provides a powerful diagnostic to constrain particle size distributions.

Downloaded From: http://astronomicaltelescopes.spiedigitallibrary.org/ on 01/14/2017 Terms of Use: http://spiedigitallibrary.org/ss/termsofuse.aspx

on the ground, and for the HST Faint Object Spectrograph, is to employ a single Wollaston prism, as in the baseline design, with a rotatable half-wave plate ahead of the prism for sequential imaging in pairs. A half-wave plate rotates the polarization vector by 2× the rotation angle of the plate, so images obtained with half-wave plate angles of 0, 22.5, 45, and 67.5 deg will yield polarization state images at 0, 45, 90, and 135 deg, sequentially.

Alternatively, two Wollaston prisms (W1 and W2) can be used, each in turn (inserted into the high-contrast beam) producing images in orthogonal (o, e) polarizations imaged simultaneously side by side on the detector. The second prism is rotated 45 deg with respect to the first, so together two pairs of polarimetrically analyzed images are produced as follows: W1 (0 deg, 90 deg), which produces Stokes Q, and W2 (45 deg, 135 deg), which produces Stokes U. This will allow (for greater simplicity) nonmultiplex use of the two prisms, i.e., sequentially imaging the W1 (0 deg, 90 deg) and W2 (45 deg, 135 deg) image pairs on the detector (at different locations); this is the EXCEDE concept approach.[50] In principle, all four images could be simultaneously acquired by inserting equal-intensity beam-splitting optics ahead of W1 and W2 (which can present a challenge for induced instrumental polarization).

For completeness, a three–analyzer angle approach uses a set of three linear polarizers oriented by 60 deg (or 120 deg) relative to each other to produce a set of three polarimetrically analyzed images: $I_{0\ \mathrm{deg}}$, $I_{60\ \mathrm{deg}}$, and $I_{120\ \mathrm{deg}}$. The simplest method is for sequential measures, selecting each of the three linear polarizers in turn (e.g., on a mechanism wheel). This was the successful approach to HST coronagraphic polarimetry.

The above describes some conceptual configurations for full-linear Stokes polarimetry in a single spectral channel. In general, Wollaston prisms will exhibit chromatic aberration for bandpasses $> \sim 20\%$. Accommodating two widely separated bandpasses may require additional polarizer optics. Spectrally splitting after a single Wollaston prism (rather than before two Wollaston prisms) could be challenging, as achromatizing a single prism over an ∼2× wavelength range could pose an insurmountable image quality challenge.

One can also achieve full-linear Stokes polarimetry with a single analyzer angle fixed in the frame of the detector by rolling the telescope to change the image orientation formed on the detector. This may not be possible for some (or any) target pointings at a single epoch due to spacecraft pointing constraints. If so, it may be possible to revisit targets at separate epochs (e.g., months apart) to allow the sky to reorient relative to the spacecraft nominal roll over time. One consideration in this latter scenario is that the revisit timescale must be shorter than the Keplerian timescale for significant motion of either an exoplanet or the smallest debris dust clumps resolvable, since the target polarization fraction is scattering phase angle dependent.

8.5 *Image Contrast Augmentation with Polarimetric Point Spread Function Nulling*

Full-linear Stokes imaging polarimetry, which enables measurement of the polarized intensity ($p * I$), also, importantly, can provide contrast augmentation when imaging polarizing circumstellar material (typically about tens of percents polarization for circumstellar debris and many exoplanetary surfaces). With full-linear Stokes imaging, unpolarized coronagraphic residuals (e.g., speckles) that are correlated with the stellar light from the unpolarized ($p_{\mathrm{star}} = 0\%$) PSF halo can be suppressed, in principle, to the limit of the photon noise for a fully unpolarized star in $p * I$ imaging (where $p = p_{\mathrm{star}} + p_{\mathrm{disk}}$). This method was successfully demonstrated in space with HST coronagraphic polarimetry (e.g., Fig. 15) and works independently of, and multiplicatively with, other starlight/speckle suppression methods.

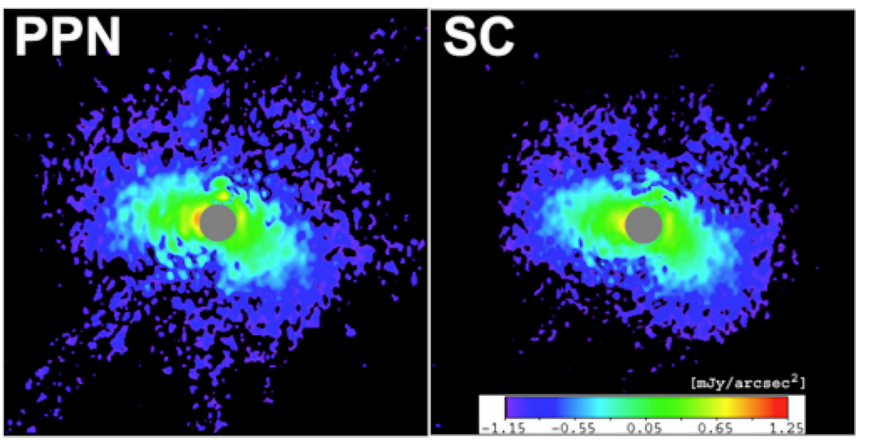

Fig. 15 (a) Polarized intensity ($p * I$) imaging of the GM Aurigae circumstellar disk from full-linear Stokes (HST/NICMOS 2.0 micron) polarimetry with polarization nulling only and (b) with speckle (PSF template) calibration and subtraction. The (input) set of raw coronagraphic polarization analysis images ($I_{0\ \mathrm{deg}}$, $I_{120\ \mathrm{deg}}$, $I_{240\ \mathrm{deg}}$), as shown in Fig. 12 (top, right), is dominated by residual unpolarized starlight in the stellar halo after incomplete coronagraphic suppression. Polarization nulling without postprocessing/speckle calibration (above, left) removes most of this residual stellar light, revealing the underlying polarized-light disk structure in a manner nearly comparable to (but without) speckle calibration (above, right). Postprocessing methods such as speckle calibration envisioned for WFIRST CGI may be combined with polarization nulling for multiplicative contrast augmentation in polarized intensity imaging (to the photon noise limit).

Downloaded From: http://astronomicaltelescopes.spiedigitallibrary.org/ on 01/14/2017 Terms of Use: http://spiedigitallibrary.org/ss/termsofuse.aspx

8.6 *Signal Requirements for Full-Linear Stokes Imaging Polarimetry*

While the linear Stokes parameters Q and U (or as normalized by the total intensity, I, such that $q = Q/I$ and $u = U/I$) follow Poisson statistics in general, the derived polarization fraction (e.g., see Ref. 51) is a positive definite quantity and follows a Rice distribution. Thus, the requirement on the per-resolution element uncertainty in the polarization fraction, p, is such that $p/\sigma_p \geq 4$. For a 50% linearly polarized source, $\sigma_u \approx \sigma_q \approx \sigma_p$, and requisite integration times for the polarimetric analysis input images (e.g., $[I_{0\ \mathrm{deg}}/I_{90\ \mathrm{deg}}]$, $[I_{45\ \mathrm{deg}}/I_{135\ \mathrm{deg}}]$ from two Wollaston prism polarimetric analyzers) must be exposed to obtain $p/\sigma_p \geq 4$. For example, in approximation, for a 12% polarized source, ~99% confidence in polarization fraction measures requires $\sigma_p < 3\%$. Approximate on-source integration time estimates can be made using the method outlined in Ref. 52. For full treatments of polarization uncertainties, see Refs. 51 and 53.

Acknowledgments

The authors are most thankful for the collaboration, helpful suggestions, and information provided by Thomas Greene on WFIRST coronagraphic instrument image simulations. The authors are grateful to M. Kuchner and C. Stark for scattered light models and use of their Zodipic code, W. Traub for details of anticipated WFIRST performance expectations and limitations, J. Krist for point spread function and coronagraphic reference data, and the members of the HST/GO 12228 team in the development of the science case discussed herein. The authors thank B. Whitney for assistance with numerical scattering models. The authors also wish to thank A. Roberge, J. Graham, H. Maness, and M. Perrin for their insightful discussions. The authors gratefully acknowledge NASA's Exoplanet Exploration Program for supporting this study on behalf of the WFIRST Science Definition Team and the Exo-S and Exo-C Science and Technology Definition Teams. This study was conducted, in part, with support to G. Schneider from NASA's Exoplanet Exploration Office.

References

1. G. Schneider et al., "Probing for exoplanets hiding in dusty debris disks: disk imaging, characterization, and exploration with HST/STIS multi-roll coronagraphy," *Astron. J.* **148**, 59–109 (2014).
2. G. Schneider et al., "NICMOS imaging of the HR 4796A circumstellar disk," *Astrophys. J. Lett.* **513**, L127–L130 (1999).
3. J. Debes et al., "Complex organic materials in the circumstellar disk of HR 4796A," *Astrophys. J. Lett.* **673**, L191–L194 (2008).
4. A. J. Weinberger et al., "The circumstellar disk of HD 141569 imaged with NICMOS," *Astrophys. J. Lett.* **525**, L53–L56 (1999).
5. M. Clampin et al., "Hubble Space Telescope ACS coronagraphic imaging of the circumstellar disk around HD 141569A," *Astron. J.* **126**, 385 (2003).
6. D. R. Ardila et al., "A dynamical simulation of the debris disk around HD 141569A," *Astrophys. J.* **627**, 986–1000 (2005).
7. M. C. Wyatt, "Spiral structure when setting up pericentre glow: possible giant planets at hundreds of AU in the HD 141569 disk," *Astron. Astrophys.* **440**, 937–948 (2005).
8. J. F. Kasting et al., "Habitable zones around main sequence stars," *Icarus* **101**, 108–128 (1993).
9. J.-C. Liou and H. A. Zook, "Signatures of the giant planets imprinted on the Edgeworth-Kuiper belt dust disk," *Astron. J.* **118**, 580–590 (1999).
10. H. H. Aumann et al., "Discovery of a shell around Alpha Lyrae," *Astrophys. J.* **278**, L23–L27 (1984).
11. B. A. Smith and R. J. Terrile, "A circumstellar disk around Beta Pictoris," *Science* **226**, 1421–1424 (1984).
12. P. Kalas et al., "A planetary system as the origin of structure in Fomalhaut's dust belt," *Nature* **435**, 1067–1070 (2005).
13. D. R. Ardila et al., "A resolved debris disk around the G2 V Star HD 107146," *Astrophys. J. Lett.* **617**, L147–L150 (2004).
14. S. M. Andrews and J. P. Williams, "Circumstellar dust disks in Taurus-Auriga: the submillimeter perspective," *Astrophys. J.* **631**, 1134–1160 (2005).
15. M. C. Wyatt et al., "Steady state evolution of debris disks around A stars," *Astrophys. J.* **663**, 365–382 (2007).
16. D. Apai et al., "The inner disk structure, disk-planet interactions, and temporal evolution in the β Pictoris system: a two-epoch HST/STIS coronagraphic study," *Astrophys. J.* **800**, 136–158 (2015).
17. M. Booth et al., "Resolved debris discs around A stars in the Herschel DEBRIS survey," *Mon. Not. R. Astron. Soc.* **428**, 1263–1280 (2013).
18. E. di Folco et al., "A near-infrared interferometric survey of debris disk stars. I. Probing the hot dust content around ϵ Eridani and τ Ceti with CHARA/FLUOR," *Astron. Astrophys.* **475**, 243–250 (2007).
19. N. D. Stock et al., "The structure of the β Leonis debris disk," *Astrophys. J.* **724**, 1238–1255 (2010).
20. K. R. Stapelfeldt et al., "First look at the Fomalhaut debris disk with the Spitzer Space Telescope," *Astrophys. J. Suppl. Ser.* **154**, 458–462 (2004).
21. M. C. Wyatt et al., "Transience of hot dust around sun-like stars," *Astrophys. J.* **658**, 569–583 (2007).
22. C. A. Beichman et al., "An excess due to small grains around the nearby K0 V star HD 69830: asteroid or cometary debris?," *Astrophys. J.* **626**, 1061–1069 (2005).
23. I. Song et al., "Extreme collisions between planetesimals as the origin of warm dust around a Sun-like star," *Nature* **436**, 363–365 (2005).
24. D. C. Hines et al., "The formation and evolution of planetary systems (FEPS): discovery of an unusual debris system associated with HD 12039," *Astrophys. J.* **638**, 1070–1079 (2006).
25. A. J. Weinberger et al., "The absence of cold dust and the mineralogy and origin of the warm dust encircling BD +20 307," *Astrophys. J.* **726**, 72–78 (2011).
26. D. Backman et al., "Epsilon Eridani's planetary debris disk: structure and dynamics based on Spitzer and Caltech Submillimeter Observatory observations," *Astrophys. J.* **690**, 1522–1538 (2009).
27. ZODIPIC2.1, http://asd.gsfc.nasa.gov/Marc. Kuchner/zodipic.2.1.tar (4 March 2016).
28. T. Kelsall et al., "The COBE diffuse infrared background experiment search for the cosmic infrared background. II. Model of the interplanetary dust cloud," *Astrophys. J.* **508**, 44–73 (1998).
29. S. S. Hong, "Henyey-Greenstein representation of the mean volume scattering phase function for zodiacal dust," *Astron. Astrophys.* **146**, 67–75 (1985).
30. J. Krist, Let Propulsion Laboratory, Private communication (2014).
31. C. Saffe et al., "On the ages of exoplanet host stars," *Astron. Astrophys.* **443**, 609–626 (2005).
32. H. Maness et al., "Hubble Space Telescope optical imaging of the eroding debris disk HD 61005," *Astrophys. J.* **707**, 1098–1114 (2009).
33. G. Benedict et al., "The extrasolar planet ϵ Eridani b: orbit and mass," *Astrophys. J.* **132**, 2206–2218 (2006).
34. J. Wisdom, "The resonance overlap criterion and the onset of stochastic behavior in the restricted three-body problem," *Astrophys. J.* **85**, 1122–1133 (1980).
35. M. C. Wyatt et al., "How observations of circumstellar disk asymmetries can reveal hidden planets: pericenter glow and its application to the HR 4796 disk," *Astrophys. J.* **527**, 918–944 (1999).
36. G. Schneider et al., "Discovery of an 86 AU radius debris ring around HD 181327," *Astrophys. J.* **650**, 414–431 (2006).
37. C. S. Stark et al., "Revealing asymmetries in the HD 181327 debris disk: a recent massive collision or interstellar medium warping," *Astrophys. J.* **789**, 58–74 (2014).
38. M. D. Perrin et al., "Imaging polarimetry of protoplanetary and debris disks," in *Polarization of Stars and Planetary Systems*, L. Kolokolova, J. Hough, and A. C. Levasseur-Regourd, Eds., pp. 244–264, Cambridge University Press, London (2015).
39. A. Cotera et al., "High-resolution near-infrared images and models of the circumstellar disk in HH 30," *Astrophys. J.* **556**, 958–969 (2001).

Downloaded From: http://astronomicaltelescopes.spiedigitallibrary.org/ on 01/14/2017 Terms of Use: http://spiedigitallibrary.org/ss/termsofuse.aspx

40. K. Wood et al., "The spectral energy distribution of HH 30 IRS: constraining the circumstellar dust size distribution," *Astrophys. J.* **564**, 887–895 (2002).
41. D. C. Hines et al., "Analysis of polarized light with NICMOS," *Publ. Astron. Soc. Pac.* **112**, 983–995 (2000).
42. H. Kimura et al., "Light scattering by cometary dust numerically simulated with aggregate particles consisting of identical spheres," *Astron. Astrophys.* **449**, 1243–1254 (2006).
43. M. D. Perrin et al., "The case of AB Aurigae's disk in polarized light: is there truly a gap?," *Astrophys. J. Lett.* **707**, L132–L136 (2009).
44. J. R. Graham et al., "The signature of primordial grain growth in the polarized light of the AU Microscopii debris disk," *Astrophys. J.* **654**, 595–605 (2007).
45. G. Schneider et al., "NICMOS coronagraphic observations of the GM Aurigae circumstellar disk," *Astron. J.* **125**, 1467–1479 (2003).
46. C. Pinte et al., "Probing dust grain evolution in IM Lupi's circumstellar disc. Multi-wavelength observations and modelling of the dust disc," *Astron. Astrophys.* **489**, 633–650 (2008).
47. K. J. Walsh et al., "A low mass for Mars from Jupiter's early gas-driven migration," *Nature* **475**, 206–209 (2011).
48. The Grand Tack, 2011, http://www.boulder.swri.edu/~kwalsh/GrandTack.html (4 March 2016).
49. D. M. Stam et al., "Using polarimetry to detect and characterize Jupiter-like extrasolar planets," *Astron. Astrophys.* **428**, 663–672 (2004).
50. O. Guyon et al., "The exoplanetary circumstellar environments and disk explorer (EXCEDE)," *Proc. SPIE* **8442**, 84421S (2012).
51. J. F. L. Simmons and B. G. Stewart, "Point and interval estimation of the true unbiased degree of linear polarization in the presence of low signal-to-noise ratios," *Astron. Astrophys.* **142**(1), 100–106 (1985).
52. W. B. Sparks and D. J. Axon, "Panoramic polarimetry data analysis," *Publ. Astron. Soc. Pac.* **111**, 1298–1315 (1999).
53. L. Montier et al., "Polarization measurement analysis. II. Best estimators of polarization fraction and angle," *Astron. Astrophys.* **574**, A136–A156 (2015).

Glenn Schneider is an astronomer (senior research scientist) at the University of Arizona's Steward Observatory (Department of Astronomy). His investigatory research is focused on the formation, evolution, properties, architectures, and diversity of (potentially) exoplanet-hosting circumstellar environments (i.e., protoplanetary, transitional, and debris disks), enabled in particular through high-contrast space-based coronagraphic imaging. He is currently PI for a NASA Explorer technology maturation project (EXCEDE) proposed to advance this line of inquiry following up his many HST investigations.

Dean C. Hines is a scientist at the Space Telescope Science Institute (STScI). He uses visible and infrared (high-contrast) imaging, spectro- and imaging polarimetry, spectroscopy, and radio imaging to investigate active galaxies, quasars, stellar evolution, and the formation and evolution of planetary systems. He is a member of the JWST/MIRI instrument and science teams, and the JWST/MIRI team lead at STScI. He is the deputy PI for the proposed EXCEDE mission.

Downloaded From: http://astronomicaltelescopes.spiedigitallibrary.org/ on 01/14/2017 Terms of Use: http://spiedigitallibrary.org/ss/termsofuse.aspx